Journal of Nuclear Materials 605 (2025) 155556

Contents lists available at ScienceDirect

Journal of Nuclear Materials

journal homepage: www.elsevier.com/locate/jnucmat

Prediction of fracture toughness of a reactor pressure vessel steel in the ductile-to-brittle transition region based on a probabilistic cohesive zone model approach

Timo Metzler *, Ermile Gaganidze, Jarir Aktaa

Karlsruhe Institute of Technology (KIT), Hermann-von-Helmholtz-Platz 1, 76344 Eggenstein, Leopoldshafen, Germany

HIGHLIGHTS

- Good agreement between experimental and numerically predicted reference temperature.
- Less material volume required for numerical determination of reference temperature compared to experimental determination following ASTM E1921.
- Fracture toughness scatter underestimated by model.
- Additional statistically distributed input parameters required to further improve model predictions.

ARTICLE INFO

Keywords:
Fracture mechanics
Finite element analysis
Cohesive zone modeling
Small specimen testing
Master curve

ABSTRACT

The availability of irradiated material for the fracture-mechanical characterization of reactor pressure vessel steels in the context of surveillance programs is severely limited. Additional efforts are necessary to reduce the amount of material required for the determination of the reference temperature based on the Master Curve methodology. The objective of this study is the further development of a method for identifying the parameters of a cohesive zone model to simulate the fracture-mechanical behavior within the ductile-to-brittle transition region. A novel approach is proposed where statistically distributed numerical fracture toughness values are obtained by means of random spatial distributions of cohesive elements with either brittle or ductile fracture properties throughout the cohesive zone. Thereby, a numerical reference temperature is determined based on the ASTM E1921 standard and compared to the reference temperature obtained from tests on miniaturized CT specimens. It is shown that with the presented approach the reference temperature of a reactor pressure vessel steel can be predicted with high accuracy. Less material is required for the calibration of the model parameters than for an experimental determination of the reference temperature. Further development of the model is required to accurately predict the experimentally observed fracture toughness scatter within the transition region.

1. Introduction

The reactor pressure vessel (RPV) is an integral part of most currently active nuclear power reactors. It is crucial for nuclear safety as it shields the environment from radiation that results from nuclear fission within the reactor core. Due to their favorable mechanical and physical properties, RPVs are usually made from low-alloy ferritic steels. The main drawback of those materials is that with increasing neutron fluence, their ductile-to-brittle transition (DBT) region is shifted towards higher temperatures. This shift can pose a risk for the safe operation of the reactor due to embrittlement of the RPV. Therefore, periodic testing of the structural steels for their fracture-mechanical behavior following standards such as ASTM E1921 [1] is mandatory to monitor the toughness degradation [2–4]. Small specimen testing has become a necessity to increase the service lifetime of existing Generation II reactors, as the number of irradiated standard-sized specimens available from surveillance programs is severely limited [5,6]. Numerical models for the simulation of the fracture process can be utilized to further reduce the material requirements for future surveillance programs. The cohesive zone model (CZM) is well suited for simulating the

* Corresponding author.
E-mail address: timo.metzler@kit.edu (T. Metzler).

https://doi.org/10.1016/j.jnucmat.2024.155556
Received 19 July 2024; Received in revised form 12 November 2024; Accepted 2 December 2024
Available online 3 December 2024

fracture-mechanical behavior of ferritic steels in the DBT region, as it can be applied for both ductile and brittle fracture. With this model, damage is only considered within a cohesive zone that is connected to the bulk of the material. Failure of the cohesive elements leads to separation of the adjacent continuum elements. The mechanical behavior of the cohesive elements follows a traction-separation-law (TSL), the shape of which depends on the type of fracture simulated.

One of the limitations of the conventional CZM is that it allows only for deterministic fracture-mechanical investigations and the statistical nature of fracture in the transition region is not incorporated directly into the FE model. In the unified cohesive zone approach by Chakraborty and Biner [7], temperature and failure probability dependent cohesive zone parameters are introduced in order to predict the ductile-to-brittle transition of RPV steels. To calibrate the model parameters for simulations in the transition region, a linear relationship is assumed between the cohesive strength and the energy release rate depending on the cumulative failure probability. The fracture toughness scatter is predicted by this assumed functional relationship, but not by the FE model itself. While the unified CZM was shown to accurately predict the fracture toughness at a given temperature and cumulative failure probability, for a complete prediction of the macroscopic fracture behavior of RPV steels, statistically distributed input parameters must be considered.

A novel probabilistic approach is presented to numerically predict the fracture toughness of RPV steels in the DBT region by modeling the cohesive zone on the mesoscale. The model can be used to generate statistical fracture toughness results in order to determine a numerical value for the reference temperature T_0 following the ASTM E1921 standard. Additionally, the finite element model allows for the detailed mechanical and fracture-mechanical investigation of testing geometries at every stage of loading. Compared to the experimental determination of T_0, the calibration of the probabilistic CZM is expected to require less testing material, which may contribute to reducing the cost of surveillance programs in the future. In this study, the objective is to apply the developed approach to predict the reference temperature of the RPV steel SA-508 Cl.3 and compare the result to the T_0 obtained from small specimen testing. Furthermore, the capability of the model to predict the experimentally observed fracture toughness scatter in the DBT region is assessed.

An overview of the probabilistic approach is given in Fig. 1. Initially, an existing parameter identification method by Mahler and Aktaa [8,9] is applied to determine the plastic flow curves, the cohesive strength and cohesive energy for the fracture-mechanical simulations in the transition region. The calibration of the cohesive zone parameters is based on tests using smooth and notched tensile specimens as well as miniaturized fracture-mechanical specimens. The fracture mechanics tests are performed using miniaturized compact tension (MCT) specimens to obtain T_0, which is later compared to the numerical reference temperature for model verification. Quantitative fractographic analysis is carried out by means of scanning electron microscopy (SEM) to determine the fraction of micro-void coalescence on the cleavage-dominated fracture surfaces

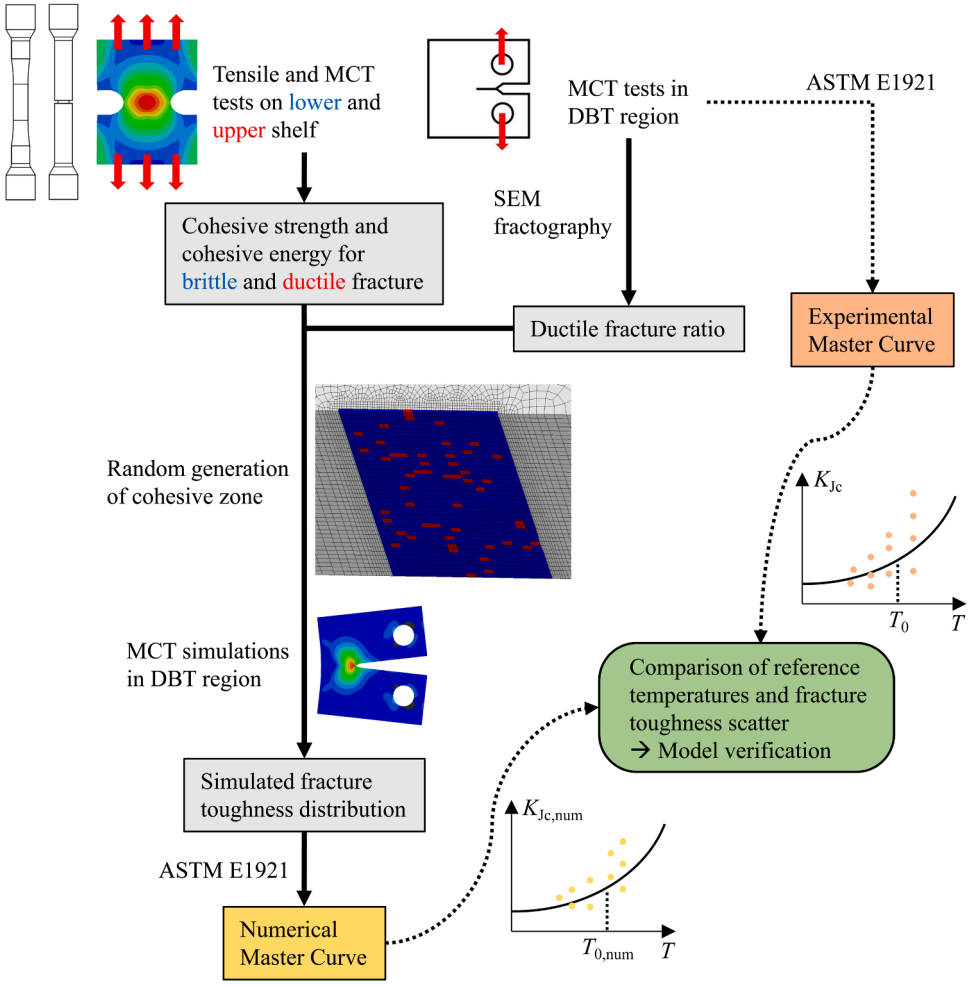

Fig. 1. Overview of the probabilistic CZM approach. First, the cohesive zone parameters and the ductile fracture ratio are calibrated by means of tensile and fracture mechanics tests with subsequent SEM fractography. Simulations in the DBT region with randomly generated cohesive zone layouts are performed to obtain statistically distributed fracture toughness values. A numerical T_0 is determined according to ASTM E1921 and compared to the experimental reference temperature for model verification.

of the MCT specimens. The resulting temperature-dependent ductile fracture ratio (DFR) is used in the calibration of the probabilistic CZM. Identification of the cohesive zone parameters is performed near the lower shelf and on the upper shelf to be able to accurately simulate both slow-stable crack growth and unstable fracture. Subsequently, meso-scale modeling of the cohesive zone is carried out for the probabilistic fracture simulations. Based on the DFR, the cohesive zone is divided into elements with ductile fracture properties that are calibrated on the upper shelf and elements with brittle fracture properties that are calibrated near the lower shelf. A random spatial distribution of the cohesive elements is generated for each simulation, leading to statistically distributed fracture toughness results. The main advantage of the probabilistic CZM is that the mean fracture behavior at any temperature in the lower DBT region can be predicted using only two sets of cohesive zone parameter calibrations. Thereby, the approach may contribute to a reduction of the material volume required for the fracture-mechanical characterization of RPV steels based on the Master Curve methodology.

2. Material

The material used for the experimental and numerical investigations in this work is the commercial low-alloy RPV steel SA-508 Cl.3 in the unirradiated condition. A block of the material was cut from the replacement closure head of the RPV of the José Cabrera power plant in Spain. The basic constituent elements of the steel are listed in Table 1. The base metal was fabricated by means of the electric furnace process. It was vacuum steam degassed, quenched and a fine grain size was produced by controlled aluminum additions.

Tensile tests on smooth round bar specimens were performed at RT and −80 °C to determine the material's yield strength σ_{YS}, ultimate tensile strength UTS and percentage reduction of area RA, which are listed in Table 2. The test temperatures were selected in order to develop one material model for simulations on the upper shelf (RT) and one for simulations near the lower shelf (−80 °C). The geometry of the specimens is shown in Fig. A.1. Young's modulus was obtained using the equation

$$E = 204 - T/16 \text{ GPa}, \quad (1)$$

which is derived in ASTM E1921 for ferritic steels.

The edge-tracing method described in [10] is applied to determine the plastic flow curves at the given test temperatures. A Pixelink CMOS camera system with a backlight is used to record the deformation of the specimen contours during testing. For testing, a universal testing machine by SCHENCK with a 63 kN load cell is used in combination with a liquid nitrogen cooled climate chamber by Instron for low temperature tests. The accuracy of the temperature control unit is within 2 °C. The average true stress and true strain are obtained from the diameter reduction in the neck. Subsequently, the Bridgman correction [11] is applied to transform the average true stress into a uniaxial true stress. The flow curves are shown in Fig. 2 and used as input for the simulations of the notched tensile specimens and the fracture-mechanical tests on MCT specimens.

3. Model parameter identification

The calibration of the cohesive zone parameters is a two-step procedure. First, tensile tests on notched round bar specimens are performed to determine the cohesive strength σ_c at both temperatures. According to Cornec et al. [12], σ_c is equal to the maximum axial stress at the experimental fracture point. The maximum axial stress is determined by simulating the tensile tests and evaluating the stress field at fracture strain. Subsequently, the cohesive energy Γ_c is used to fit the numerical force-displacement and crack growth data of the MCT simulations to the experimental results.

Table 2
Mechanical properties of SA-508 Cl.3 at RT and −80 °C.

Temperature	E [GPa]	σ_{YS} [MPa]	UTS [MPa]	RA [%]
RT	202.8	431	577	70.8
−80 °C	209.0	498	676	66.4

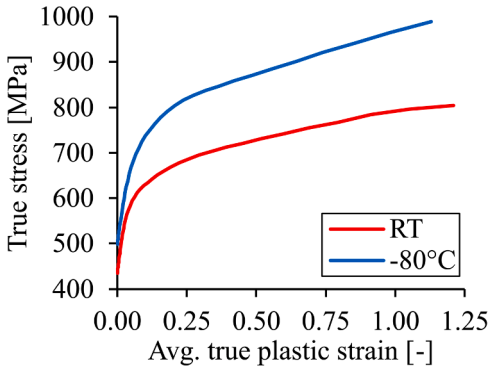

Fig. 2. Plastic flow curves of SA-508 Cl.3 at RT and −80 °C to be used for the simulations of the tensile tests and fracture mechanics tests on the upper and lower shelves.

In a study by Li and Yuan [13], it was shown based on simulations of side-grooved CT specimens that the assumption of a linear triaxiality dependence of the cohesive zone parameters significantly improves crack growth predictions in the ductile regime over simulations using constant parameters. Brocks [14] stated that the triaxiality dependence of Γ_c is negligible as the plastic strain energy is much larger than the separation energy in simulations of ductile crack growth. Furthermore, Mahler and Aktaa [9] simulated both stable crack extension and unstable fracture of T91 steel using a KLST geometry and concluded that triaxiality dependence of σ_c must be considered only if macroscopic plastic deformation is visible in the force-displacement curve. They showed that the numerical results are improved by using a constant σ_c if unstable fracture occurs in the elastic regime. Based on these findings, triaxiality dependence of σ_c is assumed at RT, while a constant σ_c is used at -80 °C. Meanwhile, Γ_c is considered to be triaxiality independent at both temperatures.

3.1. Cohesive strength

In Fig. A.1, the geometries of the notched round bar specimens for the calibration of σ_c are shown. In order to evaluate the maximum axial stress at a triaxiality representing the stress state in front of the crack tip of a fracture mechanics specimen, the notch root radius should be as small as possible. Due to manufacturing constraints for the wires used for electric-discharge-machining, the notch root radius is limited to a minimum of 0.1 mm. Therefore, 0.1 mm notched round bars are used for the calibration of the constant σ_c at −80 °C. For the determination of the triaxiality-dependent σ_c at RT, tests on 0.1 mm notched round bars are complimented by tests on 0.2 mm notched round bars and the smooth

Table 1
Basic constituent elements of the RPV steel SA-508 Cl.3 (wt%, Fe balance).

Si	C	Mn	P	S	Cr	Mo	Ni	Al	Cu	V	Sn	Co	N_2	As
0.24	0.19	1.37	0.008	0.002	0.15	0.52	0.93	0.014	0.04	<0.01	0.005	0.008	0.007	0.008

round bars that were used for determining the plastic flow curves. The experimental setup described in Section 2 is used for the tests on notched round bar specimens.

The simulated axial stress and triaxiality at the point of experimental fracture are shown in Fig. 3(a) and (b) respectively for a round bar specimen with 0.1 mm notch root radius tested at RT. It can be seen that the maxima of both field quantities are located in the center of the notch where the diameter is minimal. Three notched round bars of each type and two smooth round bars were tested at RT and then simulated to obtain the triaxiality dependence of σ_c shown in Fig. 3(c). The linear dependence is fitted by

$$\sigma_c = 449.6 \cdot h + 945.8 \text{ MPa}, \quad (2)$$

where h denotes the stress triaxiality. In addition to the tensile tests at RT, a single 0.1 mm notched round bar was tested at −80 °C for the calibration near the lower shelf. At the point of experimental fracture, the σ_c obtained from the simulation is 2005.5 MPa at a triaxiality of 1.7.

3.2. Cohesive energy

Fracture-mechanical tests on the MCT geometry shown in Fig. A.2 were performed in [10,15] prior to the numerical investigations carried out in this work. The specimens were tested in the transition region at −80, −70 and −60 °C according to ASTM E1921–21 with the experimental setup described in Section 2. Three additional tests at −45 °C were performed in this work for the development of the probabilistic CZM. A reference temperature of $T_0 = -31.5$ °C was obtained from a total of 22 valid K_{Jc} results. The force-displacement curves of the individual tests at -80 °C are used together with the median fracture toughness from the Master Curve to fit the numerical results by adjusting Γ_c. In addition to the fracture-mechanical tests performed in the transition region, tests on MCT specimens at RT were carried out in the current work following ASTM E1820-20 to determine J-Δa pairs for the crack resistance curve. As with the low temperature calibration, Γ_c is identified by fitting the numerical force-displacement and crack resistance curves to the experimental results.

3D quarter models of the MCT specimen, as shown in Fig. 4(a), are developed for the simulations at low temperature and RT respectively. Model reduction is achieved by applying appropriate symmetry conditions in the xy and xz-planes. Loading is introduced by rigid wedge-shaped pins, which are shown in brown. Additionally, a straight initial crack with a crack length to width ratio of $a_0/W = 0.5$ is assumed. The difference between the low temperature and the RT model is the length of the cohesive zone, which is a strip of zero-thickness cohesive elements starting from the initial crack front

($x = 0$ mm). For the RT model, the length of the cohesive zone is set to 2 mm to be able to capture extensive stable crack growth. In case of the low temperature simulations, no significant stable crack extension is expected prior to instability. To reduce the simulation time, the cohesive zone length is reduced to 0.3 mm. The calculations are performed using the finite-element software ABAQUS/Standard 2019.

The TSL shapes used for the simulations are shown in Fig. 4(b) for both −80 °C and RT. First introduced by Hillerborg et al. [16], a triangular shape is used for the low temperature simulations to facilitate

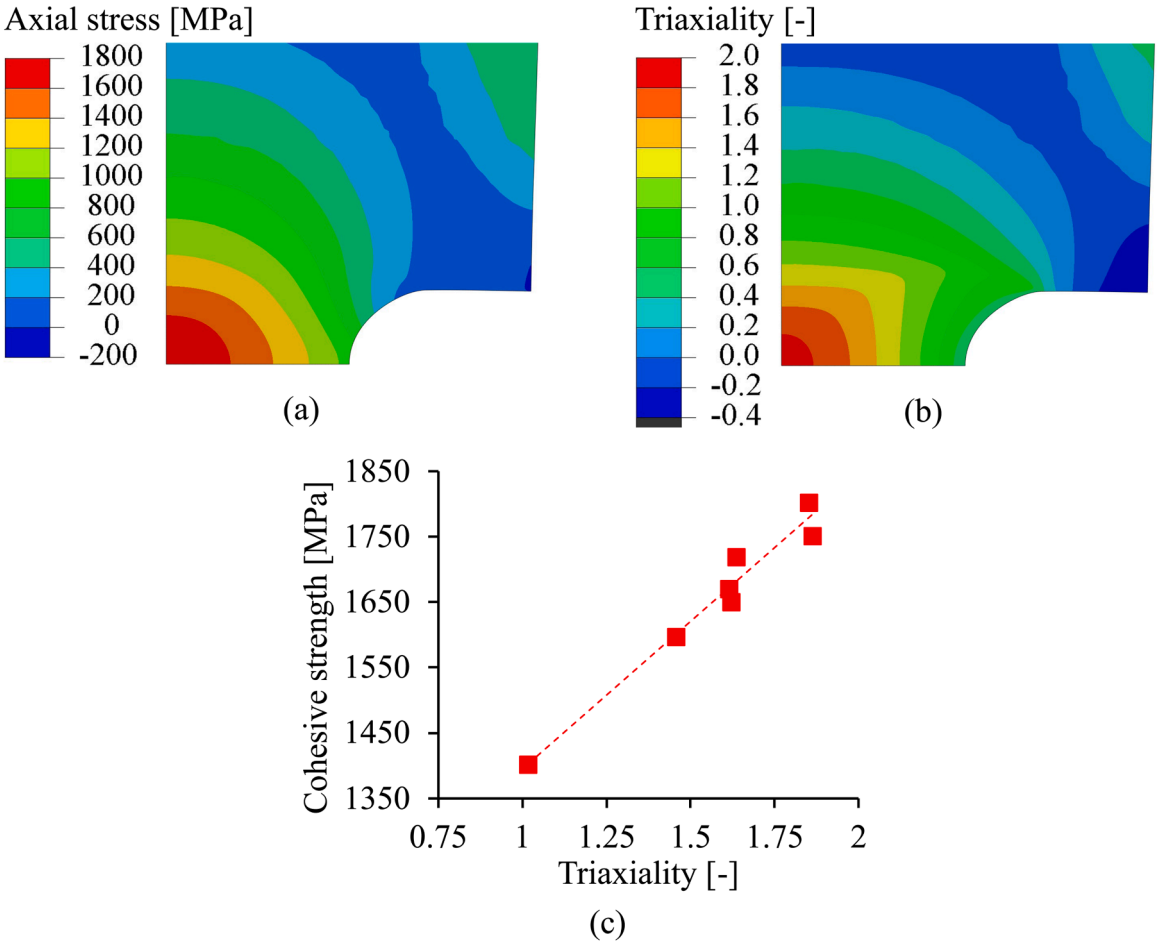

Fig. 3. Simulated axial stress (a) and triaxiality (b) at the point of experimental fracture of a round bar specimen with 0.1 mm notch root radius tested at RT. Both the maximum axial stress and the maximum triaxiality are located in the center of the specimen. (c) Cohesive strength vs. triaxiality data points from simulations of smooth and notched round bar specimens at RT. Approximately linear triaxiality dependence of the cohesive strength is obtained.

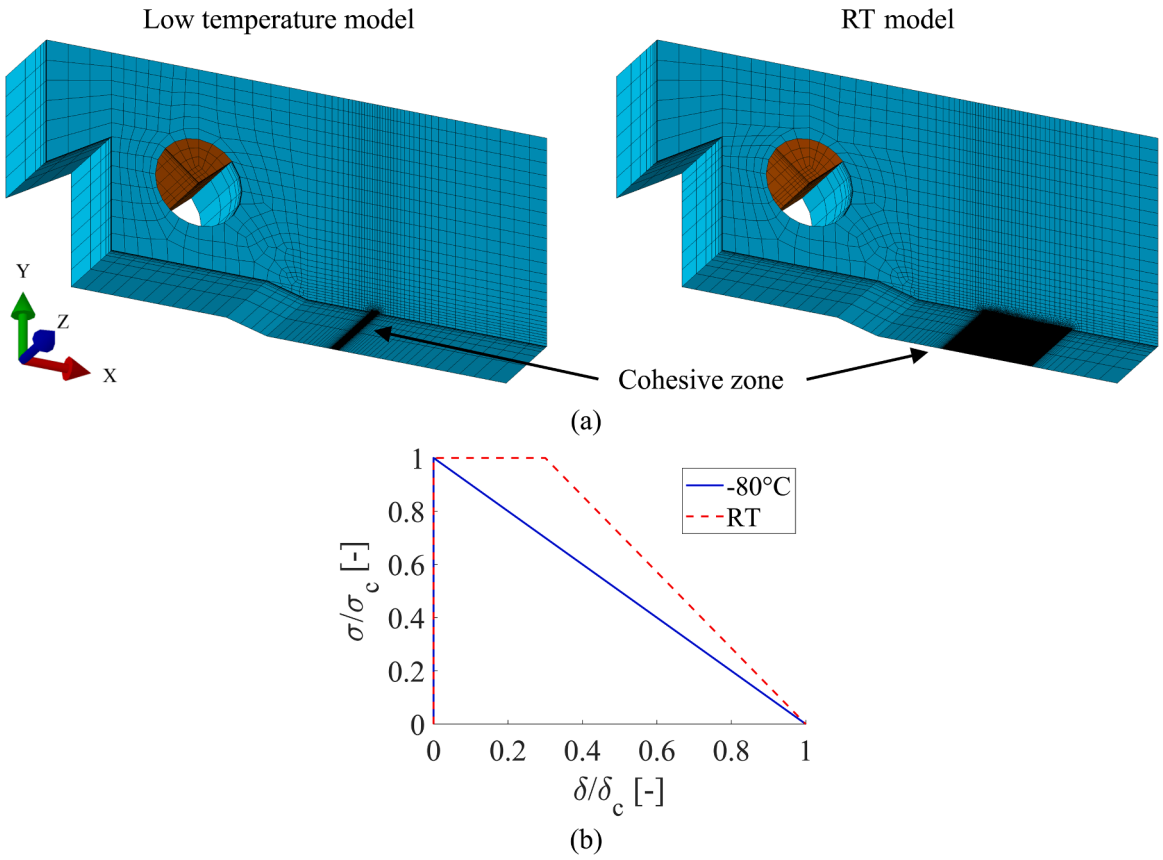

Fig. 4. (a) 3D quarter models of the MCT geometry for low temperature simulations (brittle fracture) and RT simulations (ductile crack growth). The cohesive zones are represented by the highly refined regions along the *xz* plane. (b) TSL shapes used for the fracture mechanics simulations at low temperature (−80 °C) and RT respectively. A triangular shape is used for brittle fracture at −80 °C, while a trapezoidal shape is used for ductile crack growth at RT.

unstable crack growth. The trapezoidal TSL by Tvergaard and Hutchinson (1992) [17] with a region of constant cohesive stress is used for the simulation of ductile tearing at RT. Following the recommendations by Scheider [18], a high initial stiffness is used for both models. The region of constant cohesive stress of the trapezoidal TSL extends to 30 % of the critical separation δ_c to obtain a moderate unloading slope.

An unstable crack growth criterion is required for the simulations at −80 °C to identify the point of instability where the fracture toughness K_{Jc} can be determined. In Fig. 5(a), it is shown that the simulated crack growth rate $da/dCOD$ starts to increase rapidly once σ_c is reached by the crack opening stress in front of the crack tip. Therefore, the global crack growth rate exceeding 1 mm/mm is used as the criterion for the initiation of unstable crack extension. The exact point at which this criterion is met depends on the cohesive energy, which means that the numerical fracture toughness can be precisely fitted to the experimental result by adjusting Γ_c. At −80 °C, the median fracture toughness from the experimental Master Curve, size-adjusted to a 1T CT geometry (25 mm thickness), is 79.9 MPa$\sqrt{m}$. The simulation yields a value of 79.7 MPa$\sqrt{m}$ with a cohesive energy of 0.94 N/mm. Satisfactory agreement between the experimental and numerical force-COD curves is achieved, as shown in Fig. 5(b). The average force from the experiments is slightly underestimated by the simulations.

Regarding the simulations at RT, both the experimental force-COD and crack resistance curves are fitted simultaneously. A comparison between the experimental and numerical curves is shown in Fig. 6(a) and (b) respectively. An acceptable agreement is obtained using $\Gamma_c =$

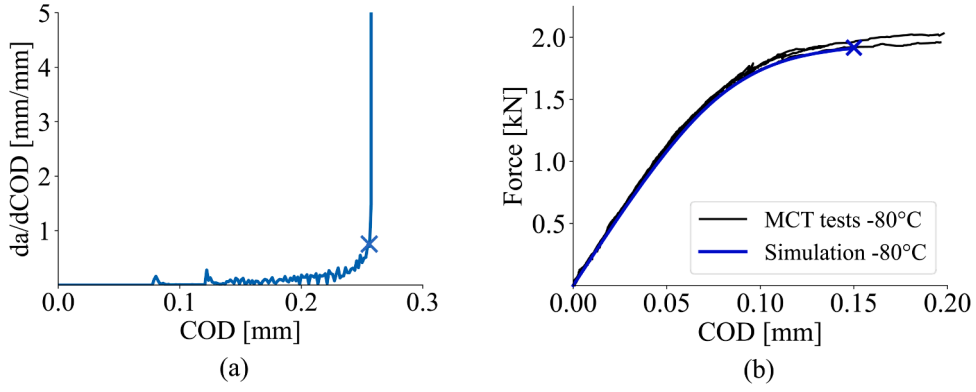

Fig. 5. (a) Simulated crack growth rate against COD showing point of unstable fracture where crack growth rate increases exponentially. (b) Experimental vs numerical force-COD curves at -80 °C showing good agreement. The numerically predicted unstable fracture points are marked by the crosses.

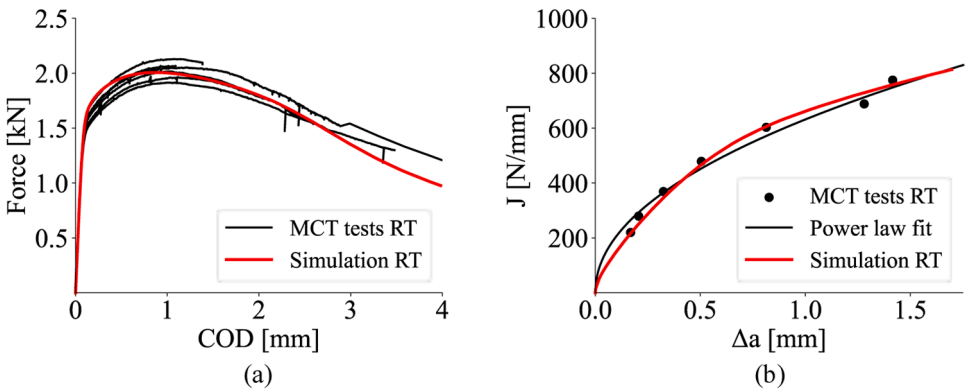

Fig. 6. (a) Experimental and numerical force-COD curves at RT showing good agreement. (b) Experimental and numerical crack resistance curves at RT showing good agreement.

2.25 N/mm, with the average experimental force being slightly overestimated by the simulation at the beginning of plastic deformation and underestimated at a COD above approximately 2.5 mm. Seven MCT specimens were tested to different displacement levels to determine J-Δa pairs according to the basic procedure of ASTM E1820–20. The simulated curve is shown to closely follow the experimental points.

3.3. Ductile fracture ratio

The DFR is required for determining the number of cohesive elements with ductile properties, which will be randomly distributed among the cohesive elements with brittle properties in the probabilistic CZM approach. Calibration of the temperature-dependent DFR is performed by quantitative fractographic analysis of the MCT specimens that were tested in the transition region to determine T_0. As shown in the SEM micrograph in Fig. 7, the fracture surfaces consist of a mixture of trans- and intergranular cleavage facets and regions of micro-void coalescence, which is commonly referred to as quasi-cleavage [19]. The transgranular cleavage facets make up most of the fracture surfaces, while the regions of ductile fracture appear as patches of dimple rupture or tear ridges along the edges of individual cleavage facets. Secondary cracking is also observed on the fracture surfaces.

In Fig. 8(a), the process for determining the DFR from an individual fracture surface is shown. High-resolution micrographs are taken in a 3 × 5 pattern in front of the tip of the fatigue pre-crack, and the respective fracture mode is identified at 16 equidistant points within each micrograph. In this way, a total of 240 data points are generated per specimen, which are assumed to be an averaged representation of the fracture surface. An example analysis for an MCT tested at −60 °C is shown in Fig. 8(b). Approximately 87 % of the fracture surface consists of transgranular cleavage facets, followed by regions of ductile fracture with 7.7 %. Secondary cracks and patches of intergranular fracture form the rest of the fracture surface.

The DFR, which is equal to the fraction of ductile fracture regions, is determined for all specimens that provided valid K_{Jc} results for the evaluation of T_0. In Fig. 8(c), the resulting temperature dependence of

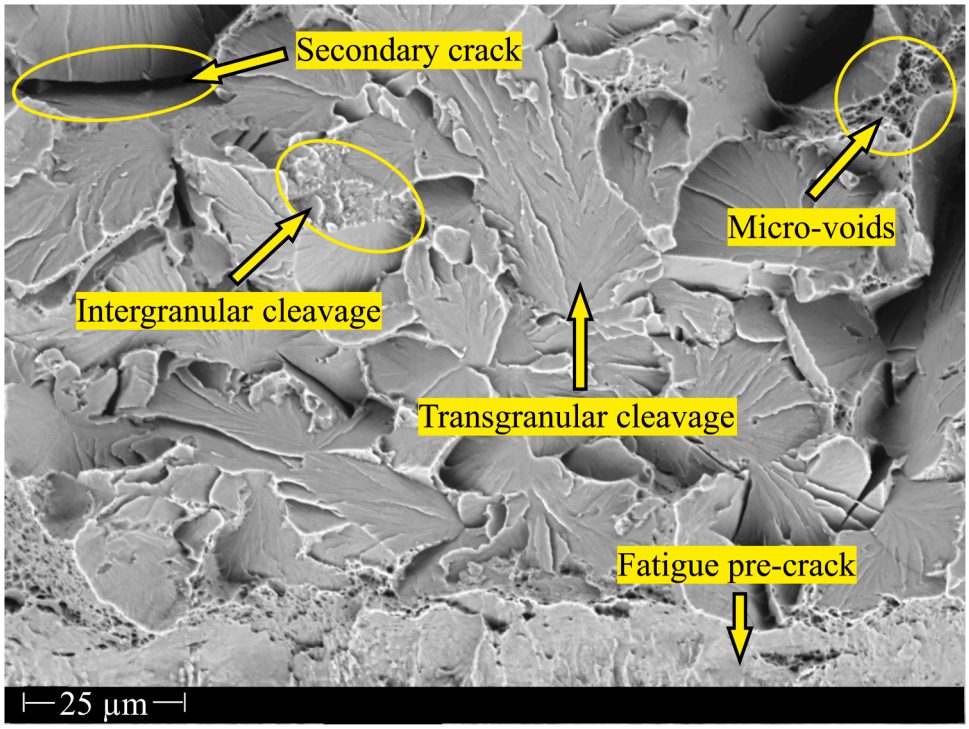

Fig. 7. SEM micrograph of a fracture surface of an MCT specimen tested at −45 °C showing multiple fracture modes: Transgranular and intergranular cleavage, micro-void coalescence, secondary cracks and the fatigue pre-crack.

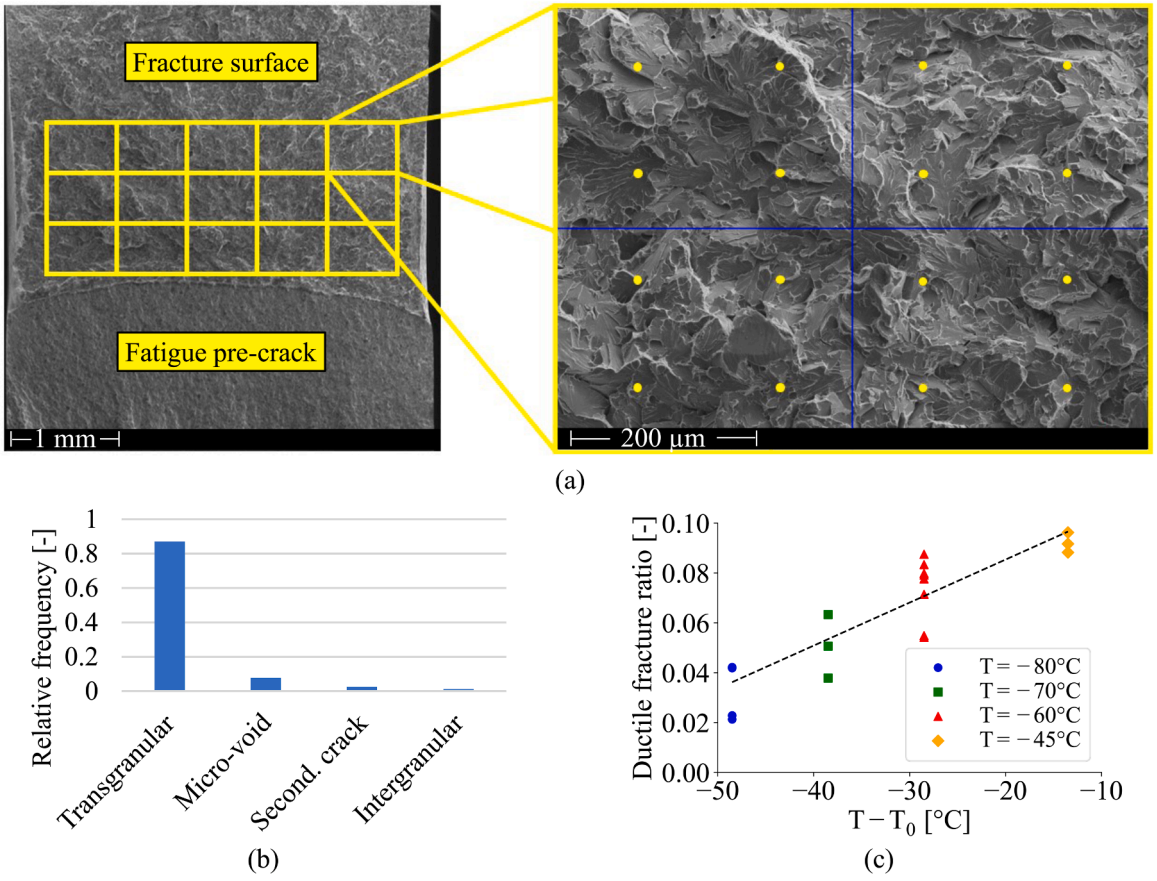

Fig. 8. (a) Procedure for determining the ductile fracture ratio. 15 micrographs are taken in a 3 × 5 grid in front of the fatigue pre-crack. Within each micrograph, the respective fracture mode at 16 individual, evenly distributed locations is evaluated to obtain a total of 240 data points. Ductile fracture ratio is defined as the number of points located within regions of micro-void coalescence divided by the total number of data points. (b) Fracture mode distribution of an MCT specimen tested at −60 °C showing that most of the fracture surfaces consist of transgranular cleavage facets, followed by regions of micro-void coalescence. (c) Temperature dependence of the ductile fracture ratio between −80 and −45 °C. While significant scatter is observed at each temperature, the mean temperature dependence is assumed to be linear.

the DFR is shown. A significant scatter is observed at the individual test temperatures with a maximum difference of 3.3 % at −60 °C. However, a positive correlation between DFR and temperature with a coefficient of determination of $R^2 = 0.77$ is obtained by means of linear regression. The regression line

$$DFR(T) = 0.00173 \cdot (T - T_0) + 0.1199 \quad (3)$$

will be used in the probabilistic CZM to control the number of cohesive elements with ductile properties in the cohesive zone.

4. Mesoscale modeling of the cohesive zone

In addition to the DFR, the shapes and sizes of a number of ductile fracture regions are measured in the quantitative fractographic analysis for modeling the layout of the cohesive zone. As shown in Fig. 7, the regions of micro-void coalescence cover a large range of sizes and can be of any shape. Due to the high computational cost of the simulations, the minimum size of the elements in the cohesive zone is limited, which means that only rectangular shapes of ductile element clusters can be modeled. It is found that the average size of the ductile fracture regions is about 50 µm in thickness direction and 18 µm in crack growth direction for all temperatures between −80 and −45 °C. Therefore, the ductile cohesive elements are grouped into clusters of the same size. This is achieved by using an element length of 50 µm in thickness direction, resulting in a total of 40 elements between the mid thickness and the side surface of the MCT, and 12 elements in crack growth direction with a respective length of 1.5 µm.

Based on the DFR, the number of cohesive elements with ductile properties, and consequently the number of ductile clusters, is determined. For instance, at −60 °C, a DFR of 0.071 is obtained from Eq. (3), meaning that 7.1 % of cohesive elements are assigned ductile properties and the rest is assigned brittle properties. In the last step, the ductile clusters are randomly distributed over the cohesive zone and the remainder of the elements are assigned brittle properties. The CZM parameters calibrated at -80 °C are applied to the brittle elements, while the parameters identified at RT are applied to the ductile elements. Examples of randomly generated cohesive zones at −80 and −45 °C are shown in Fig. 9(a) and (b) respectively. The ductile clusters are shown in red, while the blue area consists of brittle elements. Additionally, the crack growth direction is marked by the black arrows starting from the initial crack front.

5. Results

Simulations with the probabilistic CZM are performed within the DBT region at the temperatures used for the experimental determination of T_0. The number of simulations per temperature is equal to the number of corresponding MCT tests to obtain a numerical prediction of T_0 that can be compared to the experimental result. At each temperature, the respective flow curve and the DFR following Eq. (3) are used, while the CZM parameters for the ductile and brittle elements remain the same. A new spatial distribution of ductile cohesive element clusters is randomly generated for each simulation. The procedures specified in ASTM

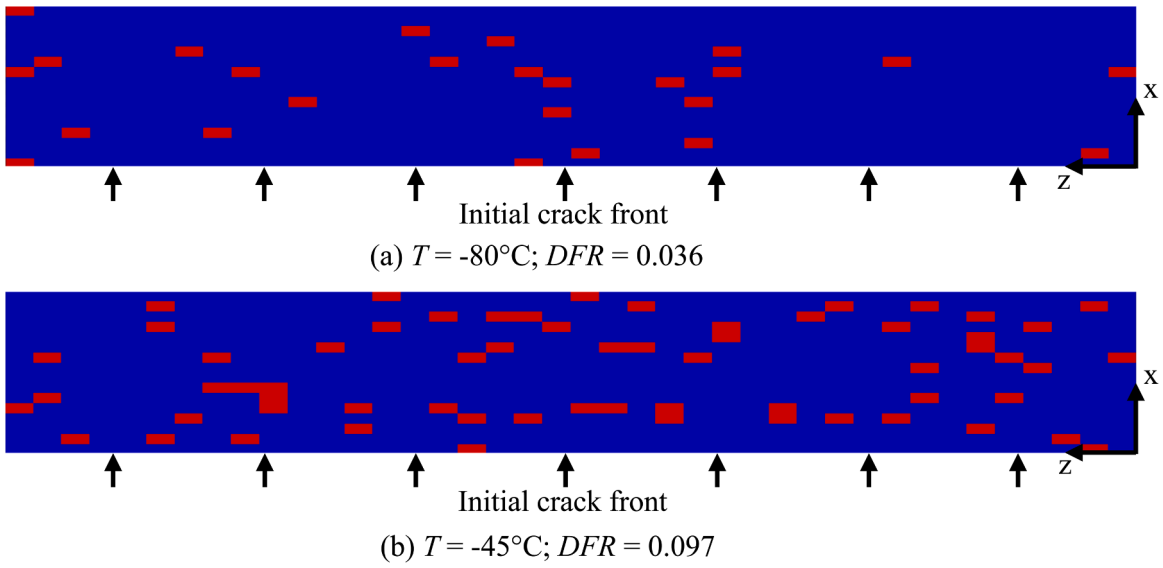

Fig. 9. Examples of randomly generated cohesive zones using the averaged cohesive element cluster size at −80 °C (a) with a DFR of 0.036 and −45 °C (b) with a DFR of 0.097. Ductile clusters are shown in red and brittle clusters in blue. At −45 °C, individual clusters can be seen to form larger clusters due to their proximity.

E1921–21 are applied to the numerical fracture toughness predictions $K_{Jc,num}$ as if they were results from physical tests, including data censoring. For the determination of individual $K_{Jc,num}$ values the unstable fracture criterion specified in Section 3.2 is applied.

A numerical reference temperature of −32.3 °C is predicted, which is in good agreement with the experimental T_0 of -31.5 °C determined based on the experimental MCT results shown in [15] and three additional tests at −45 °C. In Fig. 10, the experimentally determined Master Curve (a) is compared to the numerical prediction (b). In addition to the Master Curves, the individual censored and uncensored fracture toughness results, the tolerance bounds at failure probabilities p_f of 5 and 95 % and the censoring limit $K_{Jc,limit}$ are shown. While the mean fracture behavior at the respective temperatures appears to be well predicted, it is clear that the considerable scatter observed experimentally is not achieved by the simulations. In Table 3, the median values $K_{Jc,1T,med}$ of the experimental and numerical size-corrected fracture toughness results and the corresponding standard deviations $\sigma_{K_{Jc,1T}}$ are listed for each test temperature. The numerical $K_{Jc,1T,med}$ are between 17 % below and 11 % above the experimental values, leading to the satisfactory prediction of T_0. However, the numerical $\sigma_{K_{Jc,1T}}$ values are between 60 and 88 % below the experimental standard deviations. In the following, the scatter of the numerical fracture toughness results is investigated further.

Table 3
Experimental and numerical median fracture toughness values and corresponding standard deviations at each test temperature.

	T [°C]	$K_{Jc,1T,med}$ [MPa$\sqrt{m}$]	$\sigma_{K_{Jc,1T}}$ [MPa$\sqrt{m}$]
Exp.	−45	99.93	27.62
Num.		90.11	3.40
Exp.	−60	76.64	23.45
Num.		81.06	5.60
Exp.	−70	62.16	6.81
Num.		56.35	1.33
Exp.	−80	54.08	9.28
Num.		44.85	3.69

To evaluate the distribution of $K_{Jc,1T,num}$ predicted by the probabilistic CZM, a statistical analysis of 50 simulations at −60 °C is performed and the probability distribution that best describes the data set is determined. The χ^2 goodness of fit test is passed by the three-parameter Weibull distribution with the probability density function

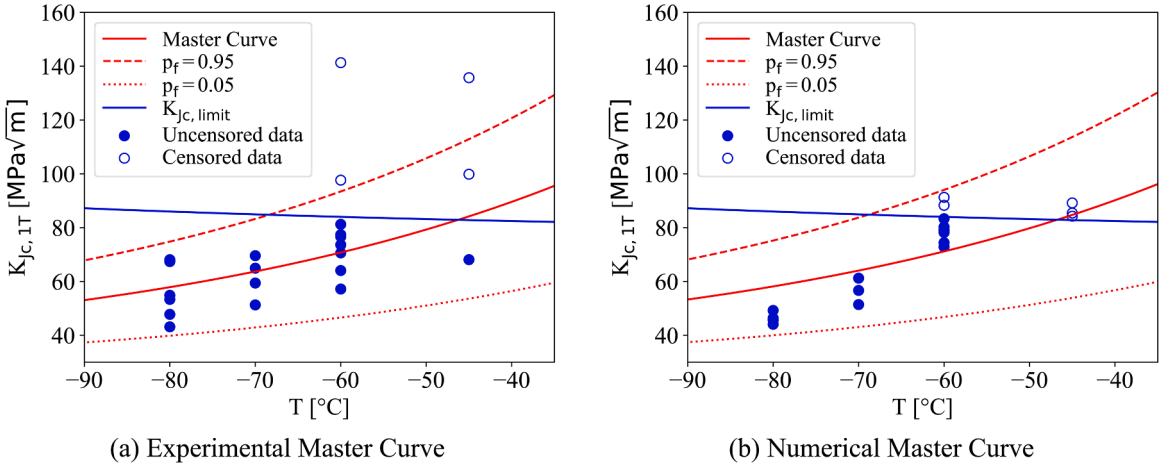

Fig. 10. (a) Experimental Master Curve obtained from 22 tests on MCT specimens with two censored test results at −60 and −45 °C respectively. (b) Numerically predicted Master Curve from 22 MCT simulations using the probabilistic CZM. Two numerical fracture toughness results were censored at −60 °C and three at −45 °C. The fracture toughness scatter at each test temperature is significantly underestimated by the model.

$$f\left(K_{\mathrm{Jc,1T,num}}\right)=\frac{m}{\left(K_0-K_{\mathrm{min}}\right)}\left(\frac{K_{\mathrm{Jc,1T,num}}-K_{\mathrm{min}}}{K_0-K_{\mathrm{min}}}\right)^{m-1}\exp\left(-\left(\frac{K_{\mathrm{Jc,1T,num}}-K_{\mathrm{min}}}{K_0-K_{\mathrm{min}}}\right)^{m}\right), \tag{4}$$

where m is the Weibull modulus, K_0 is the scale parameter and K_{min} is the threshold parameter. In Table 4, the fitted parameters of the simulated distribution are listed and in Fig. 11(a), a histogram of the 50 $K_{\mathrm{Jc,1T,num}}$ results is shown together with the curve of the probability density function. The numerical fracture toughness scatter, which covers a range between 73 and 99 MPa$\sqrt{\mathrm{m}}$, is well described by the fit.

In addition to the numerical fracture toughness distribution, the distribution of the K_{Jc} results of the nine MCT tests performed at −60 °C is evaluated. The experimental fitting parameters are listed in Table 4 and both distributions are compared to the distribution specified in the ASTM E1921 standard. In the Master Curve approach, it is assumed that the fracture toughness scatter of ferritic steels in the transition region follows a three-parameter Weibull distribution with $m = 4$ and $K_{\mathrm{min}} =$ 20 MPa$\sqrt{\mathrm{m}}$. For the given RPV steel at −60 °C, $K_0 = 75.5$ MPa$\sqrt{\mathrm{m}}$ is obtained from the experimental Master Curve. Considerable differences between the three parameter sets are observed. The Weibull modulus and scale parameter of the simulated distribution are significantly reduced compared to the ASTM distribution, while the threshold parameter is increased. Regarding the experiments, the Weibull modulus is similar to the simulated value, while the remaining parameters lie between the other distributions. It is noted that the experimental distribution may not accurately represent the statistical fracture-mechanical behavior of the material due to the small data set size of nine $K_{\mathrm{Jc,1T}}$ results.

The differences between the three-parameter Weibull distributions are highlighted by their cumulative failure probability curves, which are shown in Fig. 11(b). By the increased slope of the simulated curve, it can be seen that the numerical fracture toughness scatter is reduced compared to both the experimental and the ASTM distribution. Specifically at high cumulative failure probabilities, a large deviation is observed between the numerical and the experimental distribution due to the outliers present in the experimental data set. The fracture toughness corresponding to a cumulative failure probability of 95 % is 94.8 MPa$\sqrt{\mathrm{m}}$ for the simulated distribution, while a value of 124 MPa$\sqrt{\mathrm{m}}$ is obtained experimentally. For a cumulative failure probability of 5 %, a fracture toughness of 74.5 MPa$\sqrt{\mathrm{m}}$ is predicted by the model, which is significantly higher than the experimental value of 54.4 MPa$\sqrt{\mathrm{m}}$. Regarding a 50 % cumulative failure probability, both the numerical and the experimental distribution are shifted towards lower fracture toughness values compared to the distribution assumed in the standard. A median $K_{\mathrm{Jc,1T,num}}$ of 82 MPa$\sqrt{\mathrm{m}}$ is predicted by the simulations, while the median $K_{\mathrm{Jc,1T}}$ from the MCT tests is 79 MPa$\sqrt{\mathrm{m}}$. A median $K_{\mathrm{Jc,1T}}$ of 89 MPa$\sqrt{\mathrm{m}}$ is obtained from the ASTM distribution. This confirms that the average fracture-mechanical behavior of the material is well described by the probabilistic model.

6. Discussion

Based on the comparison of the experimental and numerical Master Curves and the statistical analysis of the numerical fracture toughness distribution, it was shown that, while the mean fracture behavior is affected by the presence of the ductile clusters in the cohesive zone, the impact of their random spatial distribution on the scatter of $K_{\mathrm{Jc,num}}$ is rather small. While the numerical fracture toughness scatter is caused exclusively by the presence of the ductile clusters, in the case of physical specimens a number of uncertainties contribute to the observed scatter. The experimentally obtained distribution of K_{Jc} in the transition region is caused primarily by brittle cleavage-initiating particles located in front of the crack tip, which are not considered in the present model. Therefore, to increase the numerical fracture toughness scatter, the next modeling step should be to introduce a small, randomly located region of reduced fracture resistance into the cohesive zone in addition to the ductile element clusters. This region can be thought of the “weakest link” triggering the initiation of unstable crack growth. The shape and size of this region can be determined based on fractographic analyses of the cleavage initiation sites found on the fracture surfaces of broken MCT specimens. Another factor that can be expected to contribute to the fracture toughness scatter is the pre-crack shape and size. According to Li et al. [20], pre-crack non-uniformity has an effect, albeit a weak one, on the fracture toughness of MCT specimens. In the present model, a straight pre-crack with fixed a_0/W is used for all simulations, while the pre-cracks of physical MCT specimens may differ considerably in both shape and size. In order to increase the numerical fracture toughness scatter, additional statistically distributed input parameters, such as the initial crack length and pre-crack curvature, should therefore also be taken into account in future iterations of the probabilistic model.

The main advantage of the probabilistic CZM compared to other approaches for modeling the ductile-to-brittle transition in ferritic steels, such as Beremin-type models [21] or the unified CZM by Chakraborty and Biner [7], is the direct numerical prediction of the statistically distributed fracture toughness. As with experimental testing, the fracture toughness distribution obtained using the probabilistic model is the result of random variations of the local fracture-mechanical properties of the material in front of the crack tip. These random variations are modeled based on the DFR, which is obtained by fractographic analysis of broken fracture mechanics specimens. In contrast to the other models, the predicted fracture toughness is therefore not dependent on statistical assumptions, but only on experimentally determined model parameters. Regarding the accuracy of the results, the probabilistic model in the present form was shown to predict the reference temperature within 1 °C of the experimental value. However, as explained above, additional development efforts are required to achieve satisfactory predictions of the fracture toughness scatter that are comparable to similar numerical models.

In addition to predicting the fracture toughness of RPV steels in the transition region, a main objective of the probabilistic approach is to require less material for the numerical determination of the reference temperature than for an experimental determination according to ASTM E1921. Experimental Master Curve evaluations of the material SA-508 Cl.3 from four different laboratories were analyzed by Naziris et al. [15], showing that of a total of 71 MCT tests, 77 % were valid and required no censoring. Within this round robin, an approximate T_0 was given as an orientation for selecting the initial test temperature. Without this orientation, it can be assumed that at least three additional tests might have been required per laboratory for finding the optimal test temperature range. Based on this data set, and assuming a minimum of eight uncensored K_{Jc} values to obtain a valid T_0, an average of 14 MCT specimens can be considered the minimum required for determining T_0

Table 4
Parameters of the numerically predicted three-parameter Weibull distribution, the distribution of the MCT test results and the distribution assumed in the ASTM E1921 standard at −60 °C.

Distribution	m [-]	K_0 [MPa$\sqrt{\mathrm{m}}$]	K_{min} [MPa$\sqrt{\mathrm{m}}$]
Simulated	1.7	11.8	72.4
Experimental	1.6	37.3	49.0
ASTM E1921	4.0	75.5	20.0

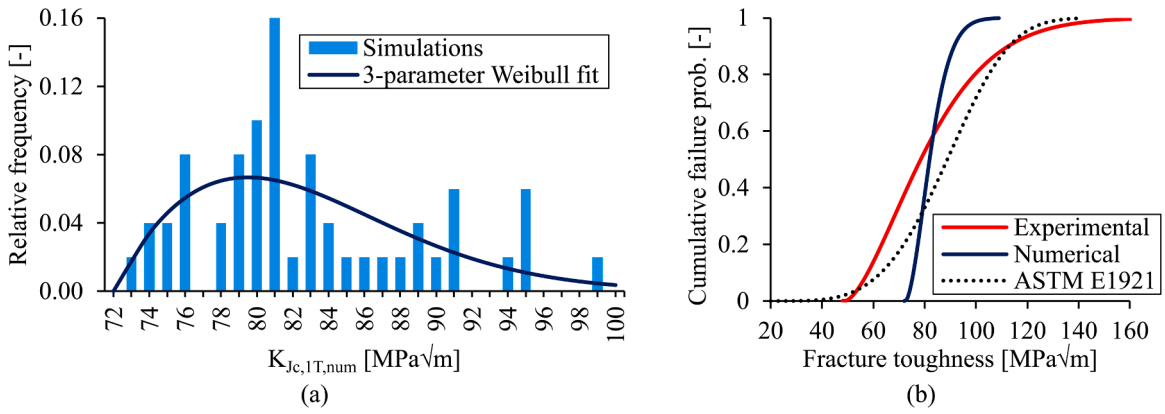

Fig. 11. (a) Histogram of 50 numerical fracture toughness results at −60 °C with fitted Weibull probability density function. The simulated values are scattered between 73 and 99 MPa$\sqrt{\text{m}}$ and their statistical distribution is well described by the fit. (b) Cumulative failure probabilities of the simulated, experimental and ASTM Weibull distributions at −60 °C. While the mean fracture toughness of the numerical distribution is comparable to the experiments, the scatter is significantly underestimated.

experimentally. Regarding the probabilistic CZM approach, smooth and notched round bar specimens are required in addition to MCT specimens to calibrate the model parameters. The flow curves are needed at each temperature of interest within the transition region and at RT, while the calibration of the cohesive zone parameters is only necessary at a temperature near the lower shelf and at RT. Besides, the determination of the DFR at multiple temperatures in the transition region is required.

In Table 5, the minimum expected number of tests of each type of specimen for the experimental determination of T_0 following the standard and for the numerical determination with the probabilistic CZM is summarized. Considering that the envelope of each round bar specimen requires about 13 % less material volume than an MCT, and assuming that probabilistic simulations are to be performed at three temperatures in the DBT region, the minimum material volume required for calibrating the probabilistic CZM corresponds to 12 MCT specimens. Consequently, the material requirement is on average lower than for an experimental determination of T_0.

The material volume required for the probabilistic CZM may increase considerably if the investigated RPV steel is inhomogeneous. However, this is also the case for an experimental determination of T_0. An advantage of the probabilistic CZM is that the MCT tests in the transition region can be used to calibrate the DFR even if the K_{Jc} results would have to be censored according to the ASTM E1921 standard. A disadvantage is the complexity of the parameter calibration procedure and the resource intensity of the simulations due to requiring a very small element size in the cohesive zone. Determining the DFR is also time-consuming, as each of the 240 points on a single fracture surface must be considered individually.

Table 5
Minimum number of tests of each type of specimen required for the experimental determination of $\boldsymbol{T_0}$ and the numerical determination with the probabilistic CZM.

Approach	Specimen type	N_{tests} [-]	Determination of
Experimental (ASTM E1921)	MCT	14	K_{Jc}
Probabilistic CZM	Smooth round bar	4	Flow curves, σ_c
	0.1 mm notched round bar	2	σ_c
	MCT	7	Γ_c, DFR

7. Conclusion

A novel probabilistic cohesive zone model approach was introduced to simulate the fracture behavior of the RPV steel SA-508 Cl.3 in the ductile-to-brittle transition region. The approach is based on randomly generated spatial distributions of cohesive elements with either brittle or ductile fracture properties throughout the cohesive zone for predicting statistically distributed fracture toughness values. Calibration of the cohesive zone parameters is required near the lower shelf and on the upper shelf in addition to a ductile fracture ratio that is identified by means of quantitative fractography. The model was shown to accurately predict the mean fracture toughness of the material at multiple temperatures in the transition region. A numerical reference temperature was determined based on ASTM E1921 that is within 1 °C of the reference temperature obtained from tests on miniaturized CT specimens. However, the model was found to significantly underestimate the experimentally observed fracture toughness scatter. At −60 °C, the scale parameter of the numerically predicted Weibull distribution is 11.8 MPa$\sqrt{\text{m}}$ compared to the experimental value of 37.3 MPa$\sqrt{\text{m}}$, indicating a lower variability of the simulated fracture toughness results. It is assumed that this underestimation is due to the fact that no fracture-initiating particles are modeled in the cohesive zone and that a straight pre-crack of constant length was used for all simulations. By considering these aspects in future model iterations, an increase of the numerical scatter can be expected.

Due to the limited availability of irradiated testing material, one of the main objectives of the probabilistic cohesive zone model approach is to reduce the material volume required for determining the reference temperature. It was shown that the calibration of the model parameters requires less material than is necessary for an experimental determination of the reference temperature based on ASTM E1921 using miniaturized CT specimens.

CRediT authorship contribution statement

Timo Metzler: Writing – original draft, Software, Methodology, Investigation, Formal analysis, Conceptualization. **Ermile Gaganidze:** Writing – review & editing, Supervision, Resources, Methodology. **Jarir Aktaa:** Writing – review & editing, Supervision, Resources, Funding acquisition, Conceptualization.

Declaration of competing interest

The authors declare the following financial interests/personal relationships which may be considered as potential competing interests:

Timo Metzler reports financial support was provided by Euratom Research and Training Programme. If there are other authors, they declare that they have no known competing financial interests or

personal relationships that could have appeared to influence the work reported in this paper.

Acknowledgements

This project has received funding from the Euratom research and training programme 2020–2024 under grant agreement No 900014. The views and opinions expressed herein do not necessarily reflect those of the European Commission.

Appendix A. Specimen geometries

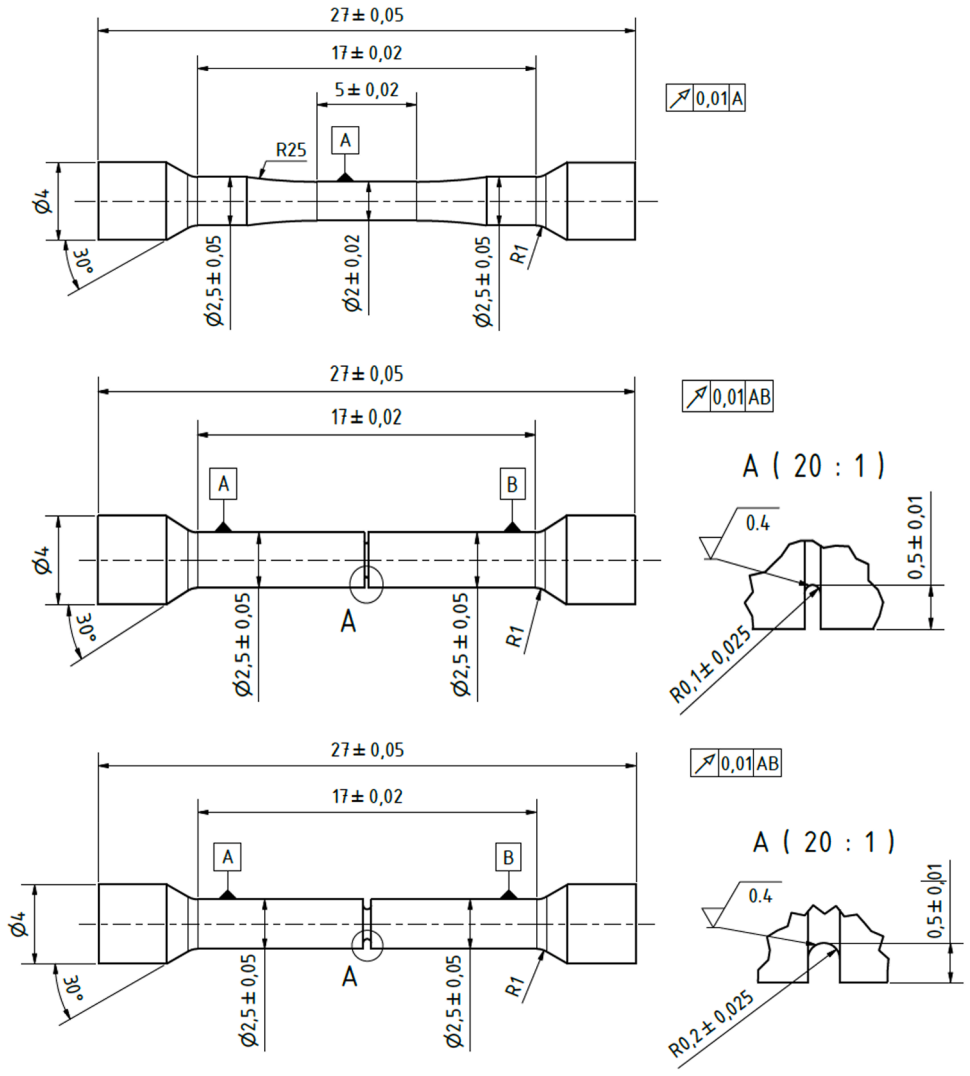

Fig. A.1. Round bar specimens for tensile testing. Specimens for tensile testing: Smooth round bar (a), 0.2 mm notched round bar (b), 0.5 mm notched round bar (c).

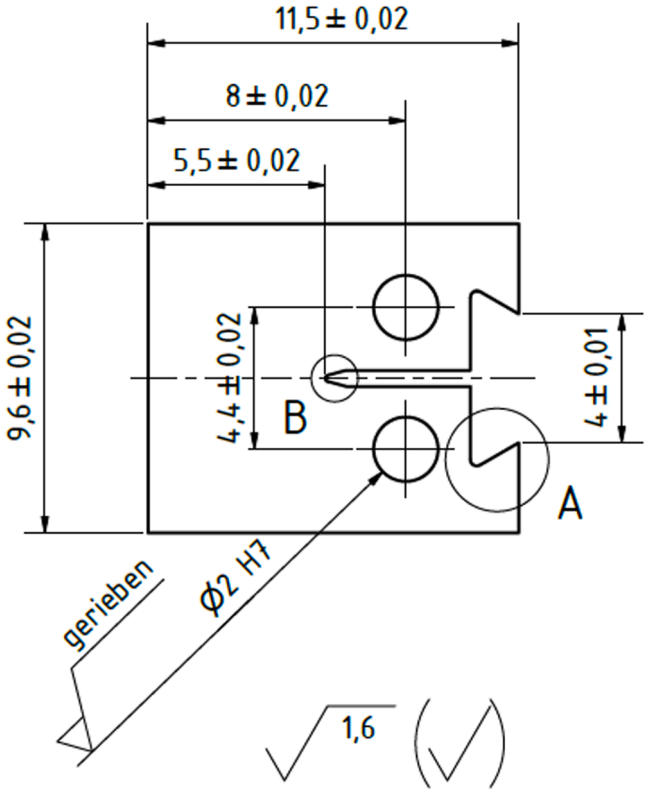

Fig. A.2. MCT specimen with 4 mm thickness for fracture mechanics testing.

Data availability

The authors do not have permission to share data.

References

[1] A.S.T.M. International, 2021. Standard Test Method for Determination of Reference Temperature, To, for Ferritic Steels in the Transition Range. E1921–21. https://doi.org/10.1520/E1921-21.

[2] IAEA, Integrity of reactor pressure vessels in nuclear power plants: assessment of irradiation embrittlement effects in reactor pressure vessel steels, in: IAEA Nuclear Energy Series No. NP-T-3.11, Int. Atomic Energy Agency, Vienna, 2009.

[3] W.L. Server, M. Brumovský, International Review of Nuclear Reactor Pressure Vessel Surveillance Programs, ASTM International, West Conshohocken, PA, 2018.

[4] IAEA, Master Curve Approach to Monitor Fracture Toughness of Reactor Pressure Vessels in Nuclear Power plants. IAEA-TECDOC-1631, Int. Atomic Energy Agency, Vienna, 2009.

[5] M. Scibetta, E. Lucon, E. van Walle, Optimum use of broken Charpy specimens from surveillance programs for the application of the master curve approach, Int. J. Fract. 116 (2002) 231–244, https://doi.org/10.1023/A:1020165900918.

[6] E. Lucon, M. Scibetta, R. Chaouadi, E. van Walle, S.W. Dean, Use of miniaturized compact tension specimens for fracture toughness measurements in the upper shelf regime, J. ASTM Int. 3 (2006) 1–16, https://doi.org/10.1520/JAI13235.

[7] P. Chakraborty, S.B. Biner, A unified cohesive zone approach to model the ductile to brittle transition of fracture toughness in reactor pressure vessels, Eng. Fract. Mech. 131 (2014) 194–209, https://doi.org/10.1016/j.engfracmech.2014.07.029.

[8] M. Mahler, J. Aktaa, Approach for Determining Fracture Mechanical Properties from Tests on Small Size Specimens at Room Temperature, Procedia Mater. Sci. 3 (2014) 434–439, https://doi.org/10.1016/j.mspro.2014.06.073.

[9] M. Mahler, J. Aktaa, Prediction of fracture toughness based on experiments with sub-size specimens in the brittle and ductile regimes, J. Nucl. Mater. 472 (2016) 178–185, https://doi.org/10.1016/j.jnucmat.2015.08.046.

[10] T. Metzler, E. Gaganidze, J. Aktaa, Numerical Prediction of Fracture Toughness of a Reactor Pressure Vessel Steel Based on Experiments Using Small Specimens, in: Proceedings of the ASME 2023 Pressure Vessels & Piping Conference - Volume 1: Codes & Standards, Atlanta, Georgia, USA, 2023, https://doi.org/10.1115/PVP2023-105918.

[11] P.W. Bridgman, Studies in Large Plastic Flow and Fracture: With Special Emphasis on the Effects of Hydrostatic Pressure, Hardvard University Press, Cambridge, MA and London, England, 1964, https://doi.org/10.4159/harvard.9780674731349.

[12] A. Cornec, I. Scheider, K.-H. Schwalbe, On the practical application of the cohesive model, Eng. Fract. Mech. 70 (2003) 1963–1987, https://doi.org/10.1016/S0013-7944(03)00134-6.

[13] X. Li, H. Yuan, Cohesive Zone Modeling for 3D Ductile Crack Propagation, Appl. Mech. Mater. 853 (2016) 132–136, https://doi.org/10.4028/www.scientific.net/AMM.853.132.

[14] W. Brocks, Cohesive Strength and Separation Energy as Characteristic Parameters of Fracture Toughness and Their Relation to Micromechanics, Str. Integr. Durab. 1 (2005) 233–243.

[15] F. Naziris, R. Hernandez Pascual, T. Metzler, E. Gaganidze, I. Uytdenhouwen, M. Kolluri, Master Curve Evaluation Using Miniature C(T) Specimens as Part of a Round Robin Program Within the FRACTESUS Project, in: Proceedings of the ASME 2023 Pressure Vessels & Piping Conference - Volume 1: Codes & Standards, Atlanta, Georgia, USA, 2023, https://doi.org/10.1115/PVP2023-107254.

[16] A. Hillerborg, M. Modéer, P.-E. Petersson, Analysis of crack formation and crack growth in concrete by means of fracture mechanics and finite elements, Cem. Concr. Res. 6 (1976) 773–781, https://doi.org/10.1016/0008-8846(76)90007-7.

[17] V. Tvergaard, J.W. Hutchinson, The relation between crack growth resistance and fracture process parameters in elastic-plastic solids, J. Mech. Phys. Solids 40 (1992) 1377–1397, https://doi.org/10.1016/0022-5096(92)90020-3.

[18] I. Scheider, The Cohesive Model: Foundations and Implementation, 2nd ed., GKSS-Forschungszentrum Geesthacht, 2006.

[19] L. Cho, P.E. Bradley, D.S. Lauria, M.L. Martin, M.J. Connolly, J.T. Benzing, E.J. Seo, K.O. Findley, J.G. Speer, A.J. Slifka, Characteristics and mechanisms of hydrogen-induced quasi-cleavage fracture of lath martensitic steel, Acta Mater 206 (2021) 116635, https://doi.org/10.1016/j.actamat.2021.116635.

[20] M. Li, I. Uytdenhouwen, T. Pardoen, R. Chaouadi, M. Lambrecht, Effect of the pre-crack non-uniformity on the initiation of brittle fracture in mini-CT specimen, Eng. Fract. Mech. 290 (2023) 109457, https://doi.org/10.1016/j.engfracmech.2023.109457.

[21] F.M. Beremin, A. Pineau, F. Mudry, J.-C. Devaux, Y. D'Escatha, P. Ledermann, A local criterion for cleavage fracture of a nuclear pressure vessel steel, Metall. Trans. A 14 (1983) 2277–2287, https://doi.org/10.1007/BF02663302.